The Sardinia Radio Telescope: a comparison between close-range photogrammetry and finite element models

The Sardinia Radio Telescope: A comparison between close-range photogrammetry and finite element models.

Dedicated to Dr. R.A. Toupin in recognition of his outstanding contribution to Mechanics.

Franco Buffa
Istituto Nazionale di Astrofisica, Osservatorio Astronomico di Cagliari, Selargius (CA), Italy
Andrea Causin
Dipartimento di Architettura Design e Urbanistica, Università degli Studi di Sassari, Alghero (SS), Italy
Antonio Cazzani
Dipartimento di Ingegneria Civile, Ambientale e Architettura, Università degli Studi di Cagliari, Cagliari (CA),
Italy
Sergio Poppi
Istituto Nazionale di Astrofisica, Osservatorio Astronomico di Cagliari, Selargius (CA), Italy
Giannina Sanna
Dipartimento di Ingegneria Civile, Ambientale e Architettura, Università degli Studi di Cagliari, Cagliari (CA),
Italy
Margherita Solci
Dipartimento di Architettura Design e Urbanistica, Università degli Studi di Sassari, Alghero (SS), Italy
Flavio Stochino
Dipartimento di Architettura Design e Urbanistica, Università degli Studi di Sassari, Alghero (SS), Italy
Emilio Turco*
Dipartimento di Architettura Design e Urbanistica, Università degli Studi di Sassari, Alghero (SS), Italy

*Corresponding author:
Emilio Turco, Dipartimento di Architettura Design e Urbanistica, Università degli Studi di Sassari, Asilo Sella, via Garibaldi 35, 07041 Alghero (SS), Italy. Email: emilio.turco@uniss.it

Abstract

The Sardinia Radio Telescope (SRT), located near Cagliari (Italy), is the world's second largest fully steerable radio telescope endowed with an active-surface system. Its primary mirror has a quasi-parabolic shape with a diameter of 64 m. The configuration of the primary mirror surface can be modified by means of electro-mechanical actuators. This capability ensures, within a fixed range, the balancing of the deformation caused, for example, by loads such as self-weight, thermal effects and wind pressure. In this way, the difference between the ideal shape of the mirror (which maximizes its performances) and the actual surface can be reduced. In this paper the authors describe the characteristics of the SRT, the close-range photogrammetry (CRP) survey developed in order to set up the actuator displacements, and a finite element model capable of accurately estimating the structural deformations. Numerical results are compared with CRP measurements in order to test the accuracy of the model.

Keywords

Sardinia Radio Telescope, finite element models, structural modeling, huge structures, active structures, high precision measurements

1. Introduction

Radio telescopes are antennas devoted to the analysis and study of celestial objects, collecting the radiation emitted in the radio region of the electromagnetic spectrum (see Figure 1). The received signals are extremely weak, thus large collecting areas are required. Moreover, the larger the size of a radio telescope, the better its angular resolution is. Nevertheless, large instruments are more sensible to deformations in their structure due to gravity, temperature and wind.

In order to contrast gravitational effects, radio telescopes may be equipped with a so-called *active-surface* (AS) system, a complex device designed to modify in real time the antenna shape.

Radio telescope deformations can be divided into spatially large-scale deformations, affecting the pointing and the focus, and small-scale deformations, which can decrease the efficiency of the telescope.

The efficiency of a radio telescope is described by the aperture efficiency η_A, see Baars [1], defined by:

$$\eta_{\mathrm{A}} = \frac{A}{A_{\mathrm{g}}}, \tag{1}$$

where A_{g} is the *geometric* area and A denotes the *effective* area, that is the area effectively contributing to collecting the incoming radiation. The aperture efficiency η_{A} takes into account many different effects; in particular, the effective area A depends on the surface-loss efficiency η_{s}, which measures the losses due to the small-scale randomly distributed deviations of the reflector from the ideal shape. It is expressed by Ruze's law [2]:

$$\eta_{\mathrm{s}} = \exp\left(-\left(\frac{4\pi\,\delta_{\mathrm{RMS}}}{\lambda}\right)^2\right), \tag{2}$$

where λ is the radiation wavelength and δ_{RMS} is the global root mean square (RMS) deviation from the ideal reflector shape, defined by:

$$\delta_{\mathrm{RMS}} = \left(\frac{1}{|\Omega|}\int_{\Omega}(\tilde{g}-g)^2\,\mathrm{d}\Omega\right)^{1/2}, \tag{3}$$

where g is the theoretical shape of the reflector and $\tilde{g}$ the actual one, while $|\Omega|$ is a measure of the surface (reflector) area.

Note that η_{s} increases as the wavelength decreases, so that surface loss efficiency becomes critical for higher frequencies. The dependence of η_{s} on δ_{RMS} implies that to maximize the efficiency (in the ideal case, to have $\eta_{\mathrm{s}} \approx 1$) a control on $\delta_{\mathrm{RMS}}/\lambda$ is required. In particular, for a good efficiency value ($\eta_{\mathrm{s}} = 53\%$), δ_{RMS} should be lower than $\lambda/16$, or at least lower than $\lambda/10$ for the minimum-acceptable efficiency value ($\eta_{\mathrm{s}} = 20\%$).

In order to correct the deformations in real time by means of the AS system, during telescope operation, a measuring technique is needed for evaluating them. Alternatively, a sensor network gathering information for their modeling and providing data to the telescope control system has to be installed.

(a) SRT view 1

(b) SRT view 2

Figure 1. SRT parts: (1) Reinforced concrete base and foundation. (2) Alidade. (3) Backup structure. (4) Principal mirror (M1). (5) Thermal shield (this is not part of the real structure although it was expected to be present in the designed one). (6) Quadrupod structure. (7) Secondary mirror (M2).

Close-range photogrammetry (CRP) is a non-contact measuring technique widely used in the radio astronomical field for the representation of the shape of large antennae. The first applications of this method to radio telescopes were the measurements of the 300 ft (91.44 m) and 85 ft (25.91 m) antennae at the National Radio Astronomy Observatory in Green Bank, West Virginia, in 1962 [3], with a camera hosted on a helicopter, achieving an accuracy of 1 mm over the 100 m size of the telescope. Afterwards, it was used in the setting of one of the 12 m diameter Atacama Large Millimeter/Submillimeter Array antennae [1], with a fully digital system achieving an accuracy of 0.030 mm.

Recently, photogrammetry methods have also been applied to the Sardinia Radio Telescope (SRT) antenna. In this paper, we aim to compare photogrammetric data, obtained during the alignment of its primary mirror [4], see Figure 2, to the finite element (FE) models of the whole structure [5].

In Section 2, a description of the SRT is presented; photogrammetric measurements are described in Section 3, while the FE numerical model and its results are presented respectively in Sections 4 and 5. Finally conclusions and new research perspectives are drawn in Section 6.

Figure 2. Setting up photogrammetric measurements at the SRT.

2. The Sardinia Radio Telescope

The SRT is a fully steerable antenna for observing the sky at frequencies between 300 MHz and 100 GHz. It has a Gregorian configuration, with a quasi parabolic shaped primary mirror (M1) and an elliptical shaped secondary mirror (M2), see again Figure 1. Its highest operating frequency, 100 GHz, corresponds to a wavelength of 3 mm. Thus, according to Ruze's law, a good efficiency value requires that the geometric deformations from its ideal shape must be kept below 0.185 mm for δ_{RMS}, or 0.3 mm if the minimum-acceptable value is taken into account. To this end, SRT is provided with an AS system [6]. The primary mirror consists of 1008 aluminum panels, and 1116 actuators with a stroke of 30 mm mounted on the backup structure. Each actuator is supported by studs and the corners of the four (or the two) nearest panels can move at the same time, in the direction normal to the local surface. They are organized in 96 radial lines with a minimum of 9 and maximum of 16 actuators for each line. Actuators work in a way that they can remove the small-scale deformations, while large-scale deformations are reduced by a correction in pointing and by secondary mirror movements.

During the construction phase, thanks to photogrammetry, panels were aligned by hand, reaching a global RMS of about 0.3 mm for the 45° telescope elevation. However, with the actuators up and running, this alignment precision may be reached over the whole elevation range, provided that panel deformation could be measured/estimated with the same or better precision.

3. Photogrammetric measurements

As stated before, CRP has been widely used throughout the whole process of SRT construction. The reason for this choice lies in its good combination of precision and survey speediness, so that CRP is preferred with respect to other survey techniques such as topographic survey with Total Station or laser tracker [4].

Indeed, CRP can reach a very high precision if a few precautions are taken. Among them:

- multi-image acquisition, taken all around the object in order to simultaneously enable camera calibration by means of a bundle adjustment procedure (in any case the use of metric cameras is mandatory), over-determination of each point of measure for outlier detection, equally distributed sigmas for the three point coordinates;
- specific signalization of measurement points with artificial targets providing unambiguous definition and automatic point identification;
- stability of environmental conditions.

Denoting by Σ_x the precision in the object with respect to the variable x, the precision in the space coordinate determination can be estimated by:

$$\Sigma_x = qm\sigma_x\,, \tag{4}$$

where m is the image scale factor, σ_x is the precision in the image space and q is a design factor depending on the geometry of the configuration, on datum orientation accuracy, on the deformation factor (spatial configuration of bundles) and on the control elements factor (accuracy of reference points). It may be the same with respect to the three spatial variables x, y and z or it may be higher along the viewing direction if the object cannot be shot from all sides.

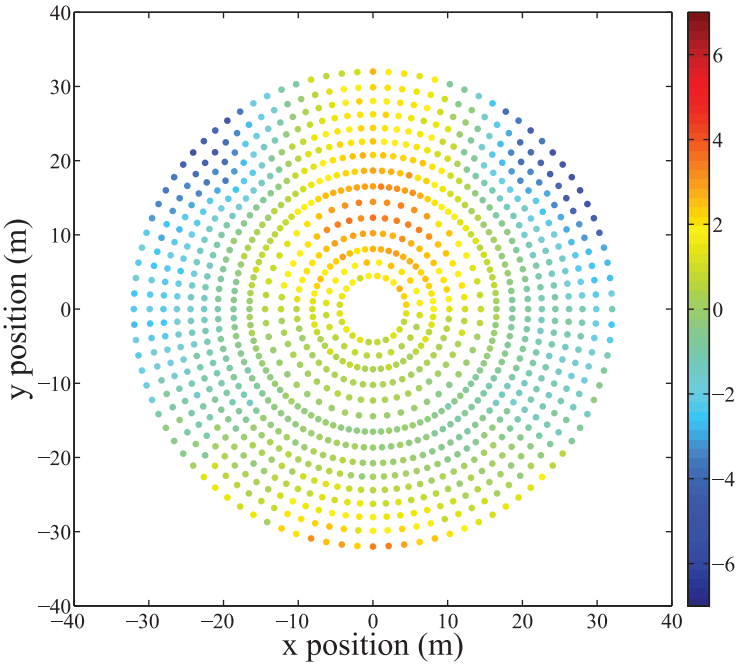

Figure 3. Graphical rendering of a CRP-deduced look-up table for displacement of each actuator at 15° elevation (chromatic scale is in mm).

Values of q may vary between 0.4–0.8 for very good configurations and up to 2–3 in weak conditions [7]. Considering an average q value of 0.6 for a good configuration, as it must be in metrological applications, and an average σ_x value of 0.08 μm, Σ_x may vary between 0.024 mm and 0.096 mm if the scale factor m varies between 500 and 2000. These values have been actually accomplished in the SRT case.

Photogrammetric measurements have been performed by the *Sigma3d Company* taking into account the different antenna parts:

1. subreflector panel alignment in which a tolerance of 0.05 mm (global RMS) was specified;
2. backup structure (BUS) deflection verification in which the structure deformation between elevation 90° and 37° had to be inside 20% of that estimated by the FE model;
3. main reflector panel alignment at 45° in which a tolerance of 0.5 mm (global RMS) was specified;
4. main reflector adjacent panels corner alignment in which a tolerance of ±0.1 mm was specified;
5. main reflector deflections at the 6 elevation positions 90°, 75°, 60°, 45°, 30° and 15°.

Of the above-mentioned tasks, only the last one is of interest for this paper. For each of the six elevations considered, a set of measurements covering the entire mirror was performed, in order to determine shape deviations from the ideal surface in a panel-wise way. The whole survey was performed during one night, in order to fulfill the environmental specifications regarding wind speed, dew point and temperature variation.

The six measurement sets were compared with the ideal surface taking into account only the small-scale displacements. To do so, a best-fitting coordinate transformation from the real to the ideal coordinates was estimated, leaving as many degrees of freedom as many real movements the telescope may do, to compensate for. The outcome of this last photogrammetric task was a look-up table containing the displacements of all the actuators, in each of the six elevation positions, computed in the normal direction to the local surface, to use them directly as movements to give in order to reach a global $\delta_{\mathrm{RMS}} = 0.3$ mm or better. Some of these look-up tables are presented in a graphic form in Figures 3 (15° elevation), 4 (60° elevation), 5 (75° elevation) and 6 (90° elevation).

4. Description of finite elements models of the Sardinia Radio Telescope

A powerful and widespread method for describing the mechanical response of a structure is the FE method [8]. It allows simulating the structural performance for a wide range of configurations/load conditions. During the

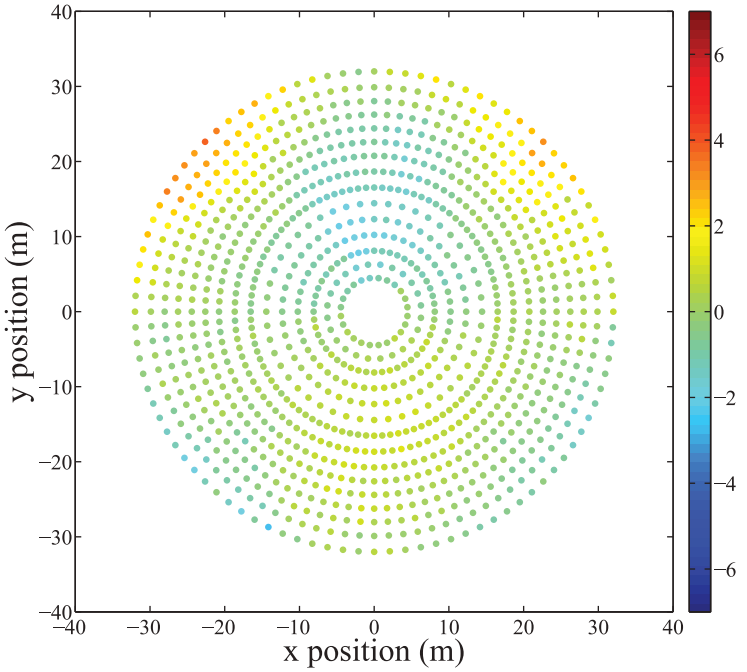

Figure 4. Graphical rendering of a CRP-deduced look-up table for displacement of each actuator at 60° elevation (chromatic scale is in mm).

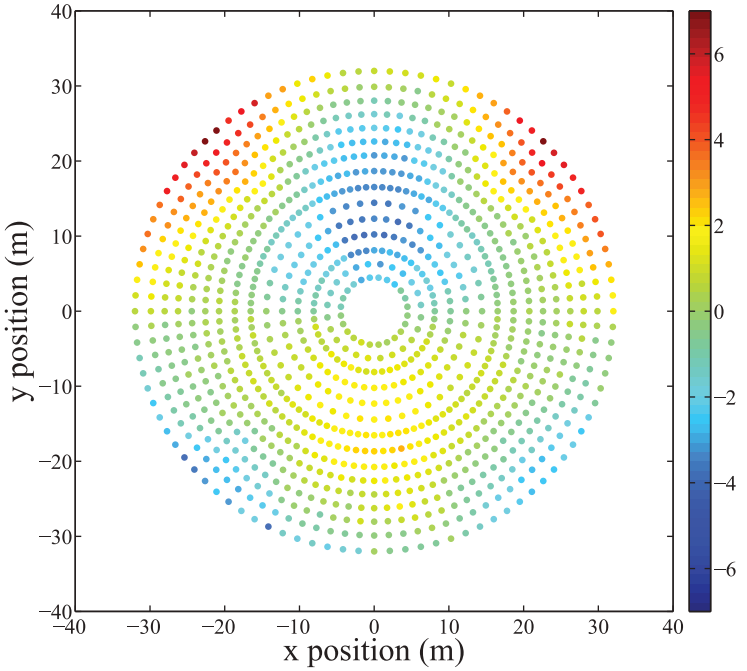

Figure 5. Graphical rendering of a CRP-deduced look-up table for displacement of each actuator at 75° elevation (chromatic scale is in mm).

design stage of the SRT several FE models were prepared. In particular, an ANSYS FE model was built by *BCV Progetti*. The last version of it (v. 37), to still include the thermal shield, which was originally designed to wrap the rear part of the backup structure is described here, see Figure 7.

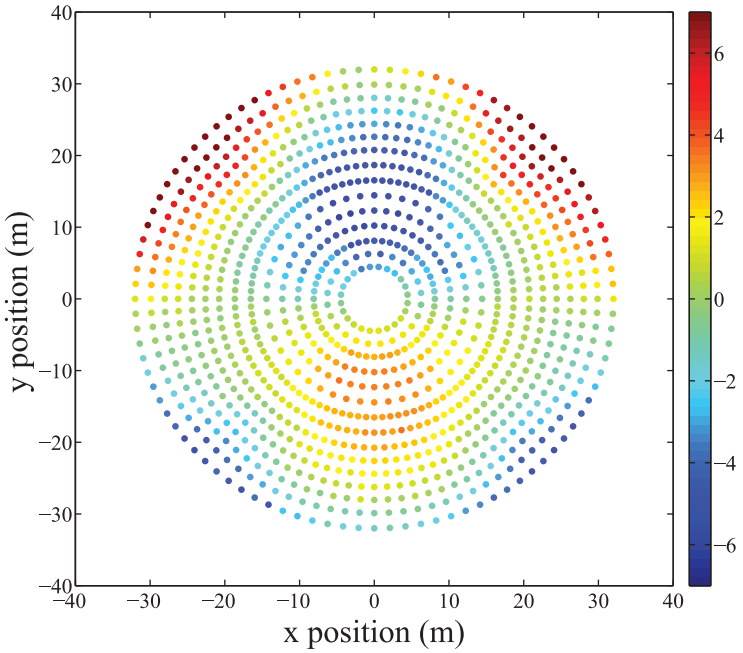

Figure 6. Graphical rendering of a CRP-deduced look-up table for displacement of each actuator at 90° elevation (chromatic scale is in mm).

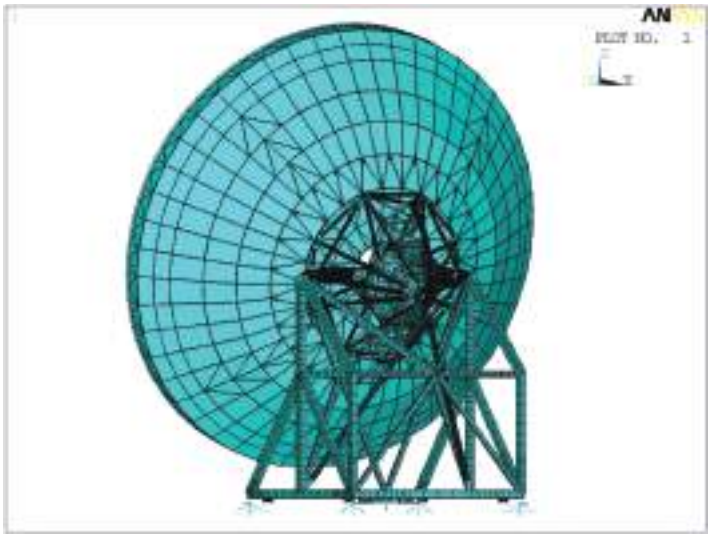

Figure 7. Back view of the SRT FE model (including the Thermal Shield) at elevation 15°.

It consists of 92,788 nodes, 94,140 elements and a total amount of 463,871 degrees of freedom. Even with such complexity, the computational cost of a linear elastic static run is quite limited and a popular personal computer can obtain the results in less than 1 min.

In a bottom-up sequence, the following parts might be singled out (see Figures 1 and 7–8):

1. *Reinforced concrete base and foundation rail*: they have been considered as perfectly rigid bodies and have not been modeled. Indeed they have been carefully designed to guarantee the verticality of the azimuth axis. Suitable displacement constraints have been inserted at the end of the base.
2. *Alidade*: represents the 3D truss structure which supports the portion of SRT (BUS, principal mirror, thermal shield, quadrupode, secondary mirror) which can tilt about the elevation axis. It is modeled by means of two-noded Timoshenko beam elements with seven degrees of freedom per node (taking into account warping, too), and by two-noded beam elements with six degrees of freedom per node. The latter

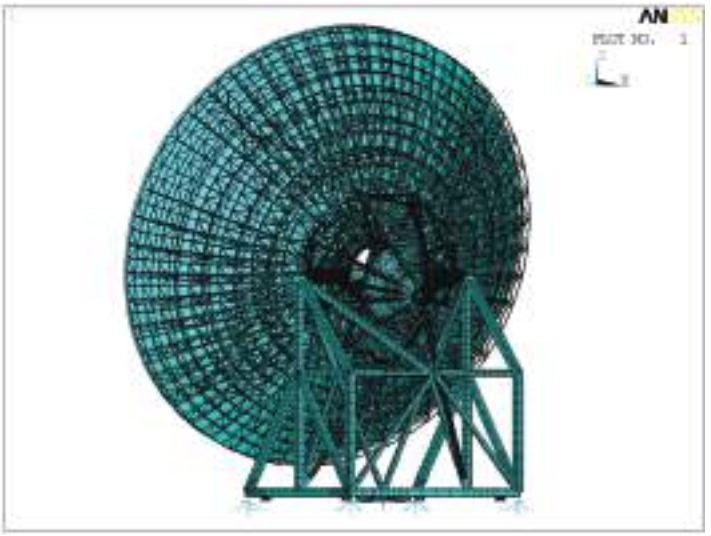

Figure 8. Back view of the SRT FE model (without the thermal shield) at elevation 15°.

group allows for independent end-release conditions, which are useful for correctly representing a 3D truss member.

3. *BUS*: the structure, shaped like a portion of an elliptic paraboloid which supports the antenna of the SRT. It is represented by a complex 3D truss system. Each structural member is modeled by at least four two-noded beam elements with six degrees of freedom at each node.
4. *Main reflector (M1)*, i.e. the principal mirror: this is placed on the front surface of the BUS and is composed of 1008 panels, each of them linked to the BUS by means of a rigid multi-point-constraint element. Any panel is represented by a single-shell element with four nodes and six degrees of freedom at each node. Only membrane stiffness is considered.
5. *Thermal shield*: this is placed on the rear surface of the BUS and is composed of 505 panels. Each panel, which is directly attached to the nodes of the BUS, is represented by a single-shell element with three or four nodes and six degrees of freedom at each node. Only membrane stiffness is considered.
6. *Quadrupod structure*: this is made of a four-legged truss structure which supports the secondary mirror. It is modeled by a mixture of two-noded Timoshenko beam elements and four-noded shell elements with six degrees of freedom per node. In this case shell elements have both bending and membrane stiffness accounted for.
7. *Secondary mirror (M2)*: only the support structure has been modeled by multi-point-constraint elements and lumped mass elements. Panels have not been explicitly modeled.

From a mechanical point of view, the steel members (alidade, BUS, quadrupod) are represented by an isotropic material model characterized by a Young's modulus $E_\mathrm{s} = 199.95\,\mathrm{GPa}$; Poisson's ratio $\nu_\mathrm{s} = 0.29464$; density $\rho_\mathrm{s} = 7908.5\,\mathrm{kg/m^3}$ and linear thermal expansion coefficient $\alpha_\mathrm{s} = 1.17\times10^{-5}\,{}^\circ\mathrm{C}^{-1}$. The principal mirror reflecting surface is composed of an aluminum alloy whose structural role is negligible and therefore has been represented by a linear isotropic material with a very low value of Young's modulus ($E_a = 0.689\,\mathrm{GPa}$), Poisson's ratio $\nu_a = 0.29$ and density $\rho_\mathrm{a} = 7086.5\,\mathrm{kg/m^3}$. Similarly, the thermal shield is made of another aluminum alloy with mechanical characteristics equal to the latter but with a different density, equal to $\rho_\mathrm{t} = 4961.9\,\mathrm{kg/m^3}$. The total weight of the model is approximately $32,259\,\mathrm{kN}$.

Considering the low-intensity loading experienced by the SRT, which for the standard calibration phase is subjected only to gravitational forces and to actuator displacements, the numerical model of the structure was formulated under the assumptions of infinitesimal strain and linear elastic behavior of all materials.

However, the thermal shield described in point 5 above, which in the design stage was expected to cover the BUS, providing thermal insulation, was not mounted on the SRT, consequently, another FE model of it, taking into account the absence of this part, has been developed by our research group, see Figure 8. For this model the number of elements decreased to 93,635 while the total number of degrees of freedom and the number of nodes remained the same. The total weight was reduced to $31,730\,\mathrm{kN}$.

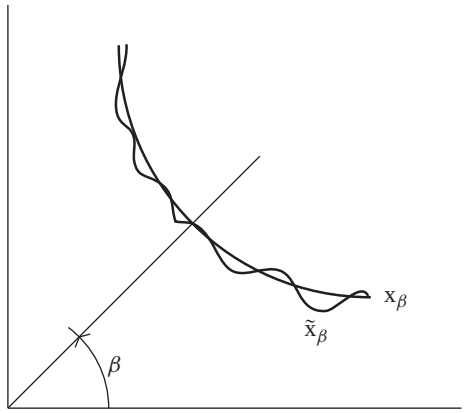

Figure 9. Sketch of the optimal $\mathbf{x}_\beta$ and actual $\tilde{\mathbf{x}}_\beta$ configuration of the the SRT.

5. Analysis of results and comparisons

CRP measurements yield a set of actuator displacements that can be interpreted as a synthetic measure of the deformation of the SRT principal mirror, see Figures 3–6. The FE models have been compared with these CRP data. Before proceeding to this comparison it is necessary to transform the FE results (which typically provide *x*-, *y*-, and *z*-components of displacements at all nodes) to components of displacements along the unit normal at all points where actuators are placed, i.e. at the corners between four panels of the principal mirror.

In order to really understand this problem it is better to depict it from a mathematical point of view: let us assume that $\mathbf{x}_\beta$ is a vector which collects points of the ideal shape of the primary mirror at elevation β, see Figure 9, and $\tilde{\mathbf{x}}_\beta$ the analogous vector collecting the corresponding positions of the same points of the actual shape. The difference $\tilde{\mathbf{x}}_\beta - \mathbf{x}_\beta$ defines the displacement vector $\mathbf{u}_\beta$ which depends on the external load and, specifically in this case, on self-weight only.

In fact, the SRT can reduce the difference between $\mathbf{x}_\beta$ and $\tilde{\mathbf{x}}_\beta$ by means of relative rigid-body motions between the primary and the secondary mirror. In formulae, the actual configuration can be described as:

$$\tilde{\mathbf{x}}_\beta = \mathbf{T}_\beta + \mathbf{R}_\beta \mathbf{x}_\beta + \Delta\mathbf{u}_\beta \,, \tag{5}$$

where $\mathbf{T}_\beta$ and $\mathbf{R}_\beta$ represent, respectively, the translation matrix and the rotation matrix (associated with this rigid-body motion), while the increment of displacement $\Delta\mathbf{u}_\beta$ comes out by depurating $\mathbf{u}_\beta$ from the above-mentioned rigid-body motion. The value of the parameters defining this rigid-body motion are determined by means of an iterative closest point (ICP) algorithm [9, 10]. This algorithm can minimize the difference between two point clouds. The reference point cloud is kept fixed, while the other one, the source, is transformed to best match the reference one. The transformation consists of a combination of a rigid rotation and translation of the source cloud. ICP iteratively revises the transformation in order to minimize the distance from the source to the reference point cloud. The *a*-th electromechanical actuator controls *p* mirror panels (where *p* can either be 2 or 4) by means of its elongation d_a. The procedure to compute the actuator's elongation works like this:

1. First the average normal vector $\mathbf{v}_a$ corresponding to the *a*-th actuator is evaluated:

$$\mathbf{v}_a = \left(\frac{1}{p} \sum_{i=1}^{p} \mathbf{n}_{a_i} \right) , \tag{6}$$

   where $\mathbf{n}_{a_i}$ is the unit vector along the normal to the *i*-th panel controlled by the *a*th actuator.
2. Then, a unit vector $\hat{\mathbf{v}}_a$ is computed from $\mathbf{v}_a$; finally, the elongation d_a results as:

$$d_a = \hat{\mathbf{v}}_a \cdot \Delta\mathbf{u}_{\beta_a} \,. \tag{7}$$

In the following sections comparison between the FE model with (denoted by 'TS') and without (denoted by 'NTS') a thermal shield and CRP data is provided in terms of such actuator elongations, evaluated point-wise

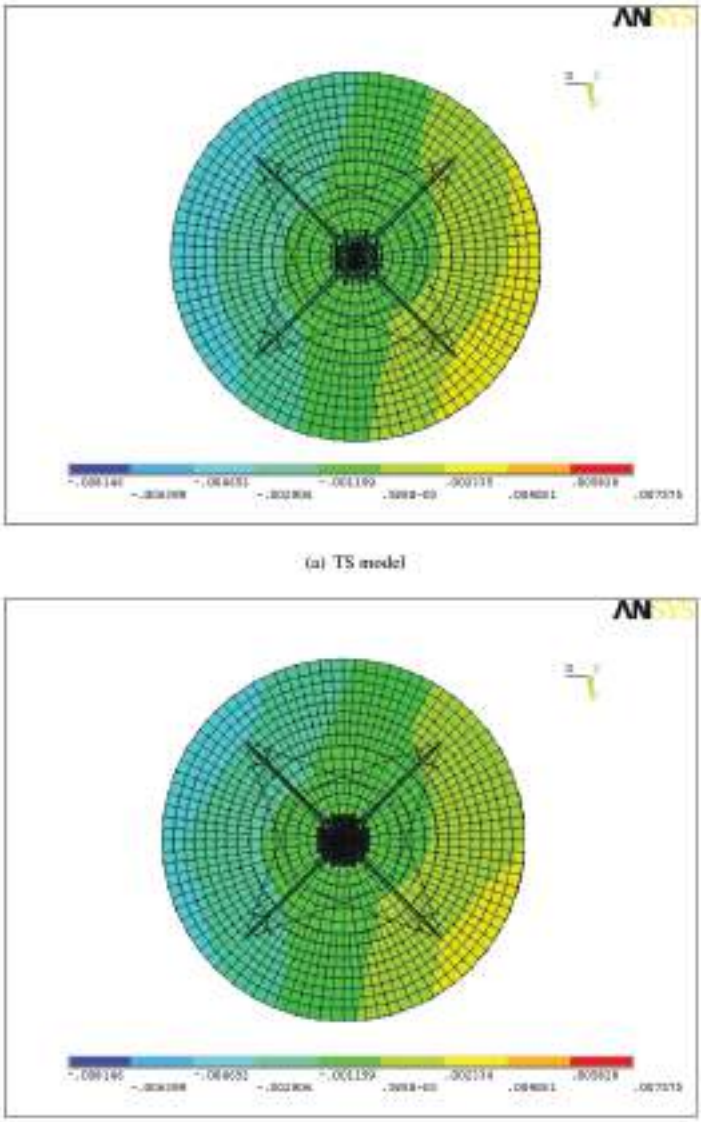

(a) TS model

(b) NTS model

Figure 10. FE model displacements along the *x*-direction at 90° elevation: view of the principal mirror (the unit of the chromatic scale is m).

and globally by means of an RMS deviation, Δ_{RMS}, defined as:

$$\Delta_{\mathrm{RMS}} = \sqrt{\frac{1}{n}\sum_{i=1}^{n}(\tilde{d}_i - d_i)^2}\,, \tag{8}$$

between two sets of n elongations $\tilde{d}_i$ and d_i. In the case of the SRT the number n of actuators belonging to the principal mirror is 1104.

5.1. Comparison between TS FE and NTS FE models

In order to develop a thorough analysis of the structural influence of the thermal shield, several comparisons between the model with and without thermal shield have been performed. For the sake of conciseness the configuration characterized by 90° elevation under gravitational loads has been considered only. In Figures 10–15 the displacements in the *x*-,*y*-, and *z*-direction are reported for the two FE models (TS and NTS). Very

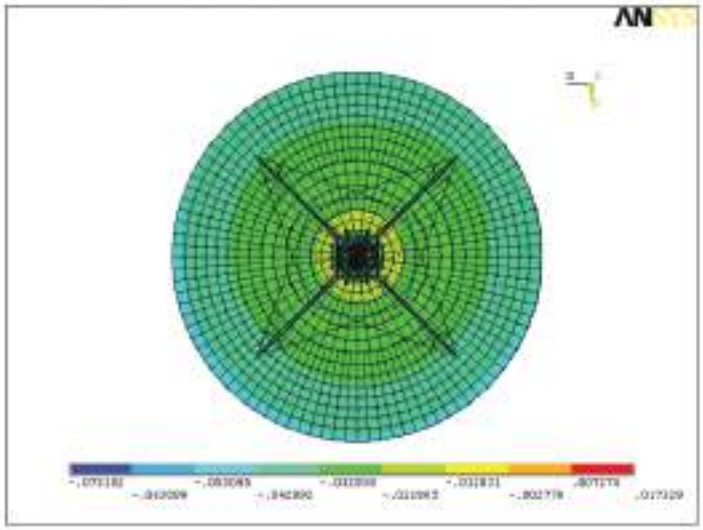

(a) TS model

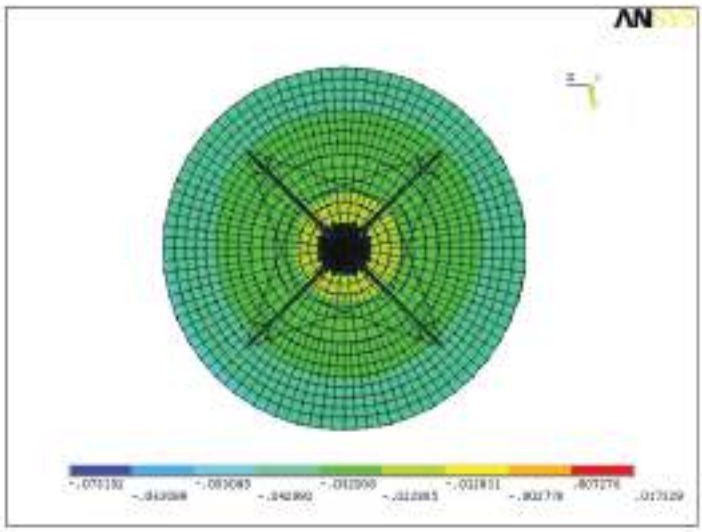

(b) NTS model

Figure 11. FE model displacements along the y-direction at 90° elevation: view of the principal mirror (the unit of the chromatic scale is m).

few differences can be seen considering the principal mirror displacements presented in Figures 10–12; these become negligible when considering a whole view like those presented in Figures 13–15. Furthermore if such global displacements are transformed into the required actuator displacements, which are necessary to correct the surface shape, (see Figure 16) the differences are still very few.

In order to highlight these differences, the actuator displacements have been evaluated for the other two elevation angles (15°, 60°) by means of the TS model (see Figure 7) and the NTS model (see Figure 8).

The local differences are reported in Figures 17–19. The chromatic scale limits are different with respect to the other sections, with the aim of highlighting the very small differences between the two models.

Figure 17 reports the situation belonging to 15° elevation where the thermal shield produces some interesting effects in the top central part of the principal mirror and on the outer circular ring. The maximum value of the local difference, defined as:

$$\Delta_{\max} = \max_{i=1,\ldots n} \mid \tilde{d}_i - d_i \mid, \tag{9}$$

is $\Delta_{\max} < 0.5$ mm, while the corresponding global Δ_{RMS} is 0.212 mm.

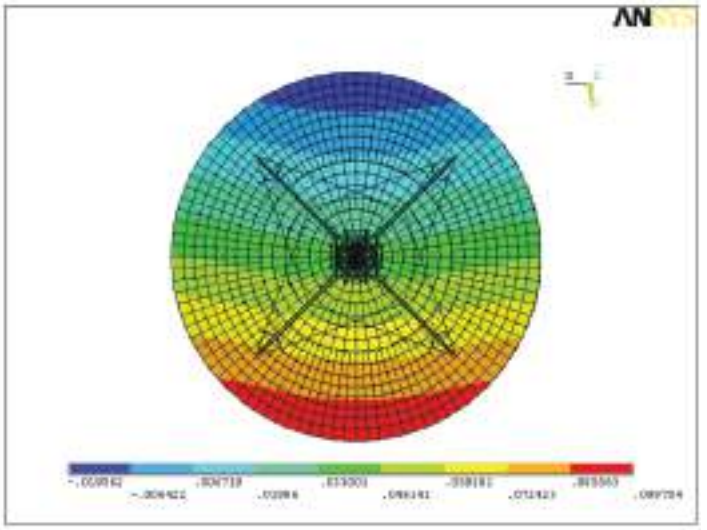

(a) TS model

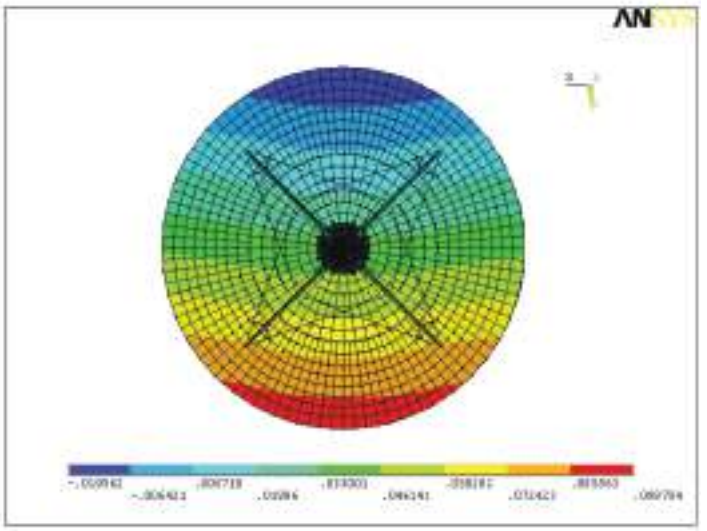

(b) NTS model

Figure 12. FE model displacements along the z-direction at 90° elevation: view of the principal mirror (the unit of the chromatic scale is m).

Figure 18 reports the 60° elevation case, where the thermal shield produces some interesting effects only on the top central part of the principal mirror. In this case, $\Delta_{\max} < 0.3$ mm and $\Delta_{\mathrm{RMS}} = 0.109$ mm.

Finally, Figure 19 reports the 90° elevation configuration corresponding to the principal mirror orthogonal to the vertical axis. In this case, the thermal shield produces a non-negligible effect on the whole principal mirror. In particular there is a characteristic symmetry between the top–bottom and inner–outer circular ring parts. This time, $\Delta_{\max} = 0.5$ mm, while the corresponding $\Delta_{\mathrm{RMS}} = 0.271$ mm.

According to the aim of this paper (FE model analysis compared to field benchmark data provided by CRP) the most important comparison between the TS and NTS models is developed in Table 1, where the deviations of actuator displacements coming from FE analysis and CRP field recordings are presented. As it was expected, the NTS model produces results more similar to CRP data than those produced by the TS model. In particular, the former provides a minimum $\Delta_{\mathrm{RMS}} = 0.491$ mm corresponding to an elevation angle of 60°, while the maximum is 0.814 mm for an elevation angle of 90°. In the case of 15°, Δ_{RMS} is 0.507 mm. The best improvement descending from assuming the NTS model instead of the TS one is obtained for the 15° elevation and

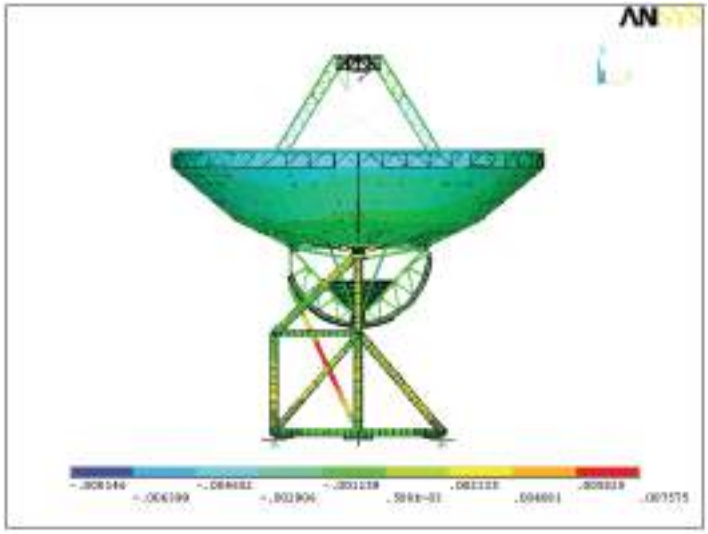

(a) TS model

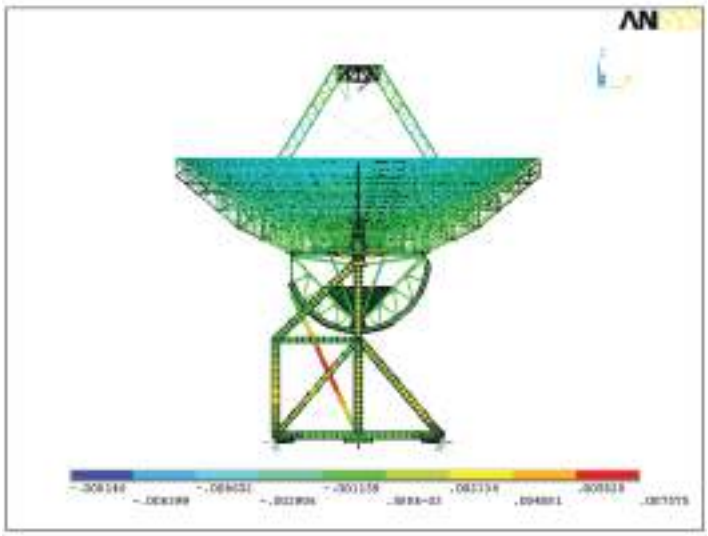

(b) NTS model

Figure 13. FE model displacements along the x-direction at 90° elevation: side view (the unit of the chromatic scale is m).

Table 1. Global RMS error of FE models compared to CRP.

Elevation β	Δ_{RMS} (mm)		% improvement
	TS	NTS	
15°	0.5751	0.5068	12
60°	0.5239	0.4907	6
90°	0.8441	0.8138	4

corresponds to 12%. This confirms the influence on the mechanical behavior of the thermal shield, which is not present in the real structure and not easily detectable by the direct absolute displacement comparisons.

5.2. Comparison between finite element models without thermal shield and photogrammetric data

As proven in the previous paragraph the FE model without the thermal shield provides the most realistic picture of the actual behavior of the SRT. Local actuator displacement errors are presented in the sequel (see Figures

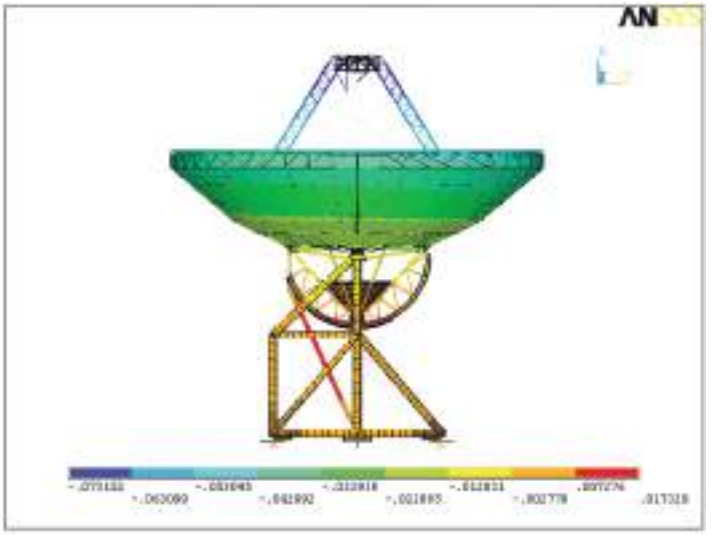

(a) TS model

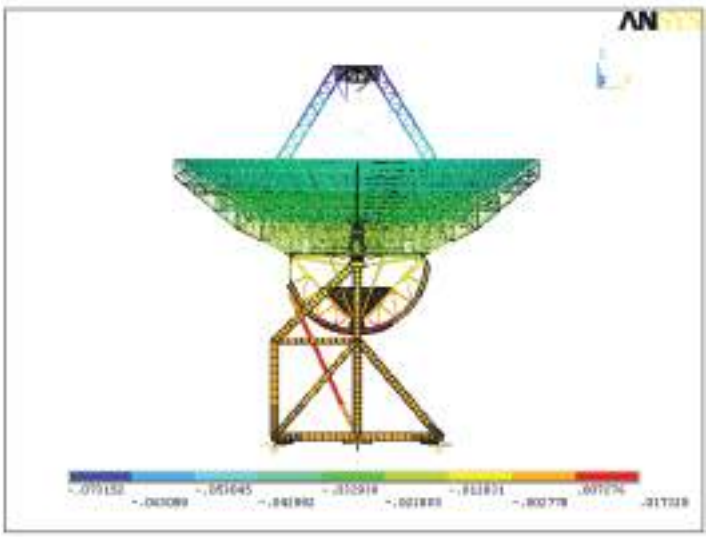

(b) NTS model

Figure 14. FE model displacements along the y-direction at 90° elevation: side view (the unit of the chromatic scale is m).

20–22). Actuator elongations have been estimated by means of the NTS FE model of the SRT, see Figure 8 for different configurations. Figures 20–22, referring to the configurations corresponding to three different elevation angles (15°, 60°, 90°), depict the local differences between the actuator displacements produced by the numerical model and CRP data. Larger differences can be observed at 90° elevation ($\Delta_{\mathrm{RMS}} = 0.814$ mm, with local differences very high in the bottom part of the mirror); while the lowest ones are seen in the 60° elevation ($\Delta_{\mathrm{RMS}} = 0.491$ mm, with a rather uniform distribution of the local differences). Probably the weight distribution when the principal mirror lies parallel to the horizon (90°) produces a structural response which is not described accurately by the model.

6. Conclusions and new research perspectives

Numerical simulations have made it evident that the FE model has to be updated in order to adequately match photogrammetric measurements. These can be considered as a kind of experimental test on the actual SRT structure. Among the extended bibliography on model updating we recall the contributions, and references

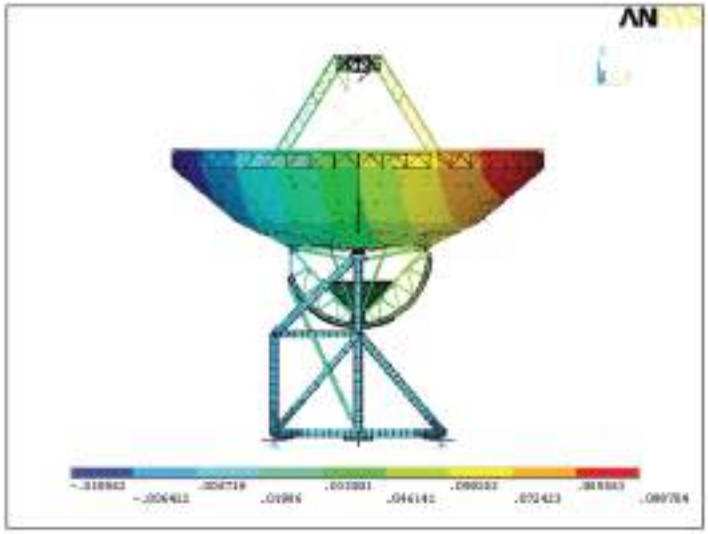

(a) TS model

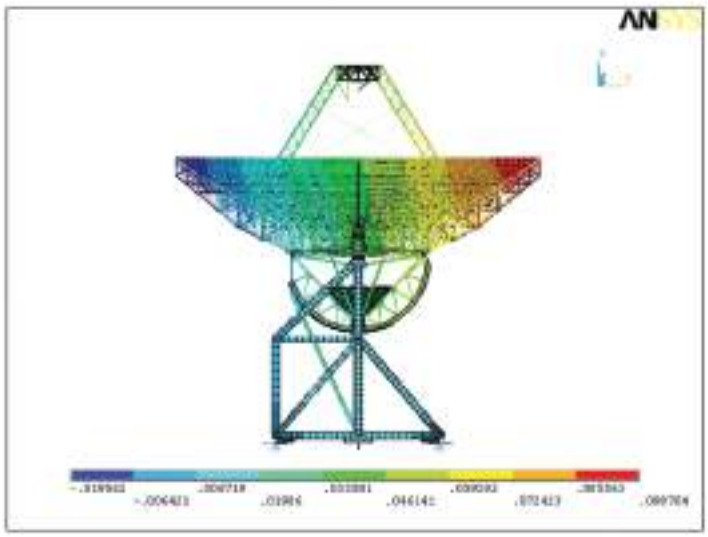

(b) NTS model

Figure 15. FE model displacements along the z-direction at 90° elevation: side view (the unit of the chromatic scale is m).

contained therein, of Friswell and Mottershead [11], Aktan et al. [12], De Sortis et al. [13] and Wang and Zhang [14] since they give the main guidelines on updating methodology and Dilena et al. [15, 16], Morassi and Polentarutti [17, 18], Bennati et al. [19], Moaveni and Behmanesh [20], Richard et al. [21], Zárate and Caicedo [22] and Schlune et al. [23] as technical applications of updating.

In Stochino et al. [24] there is a complete strategy to update the SRT FE model. Here we sketch only the main guidelines and main papers which can be profitably consulted. Updating strategies try to reduce differences between predicted data, by the FE model, and measured data, in this case by photogrammetric measurements, by a suitable procedure which has to contain an effective filter for data errors. We follow the way used by Turco [25–28] which is based on the so-called *Tikhonov approach* [29], and uses numerical tools such as singular value decomposition [30, 32, 33], and the generalized cross-validation criterion to filter the data errors, proposed in Golub et al. [34] and extensively tested by Bilotta and Turco [35, 36].

Finally, we remark that the results of this research line could also be useful to enrich refined numerical models such as those reported in Cazzani et al. [37, 38] for beams, those based on mixed and hybrid FEs [39–41], which provide more accurate stress descriptions, also in the case of layered structures [42] and those based on the so-called *isogeometric approach* [37, 38, 43, 44].

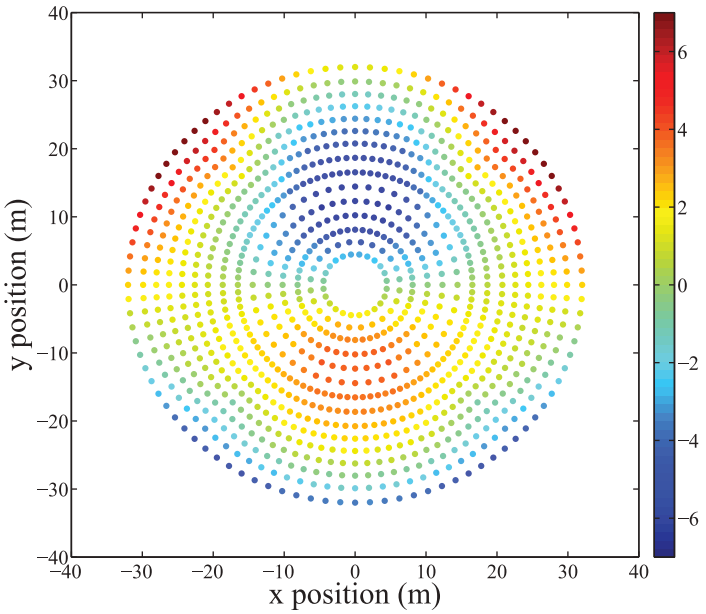

(a) TS model

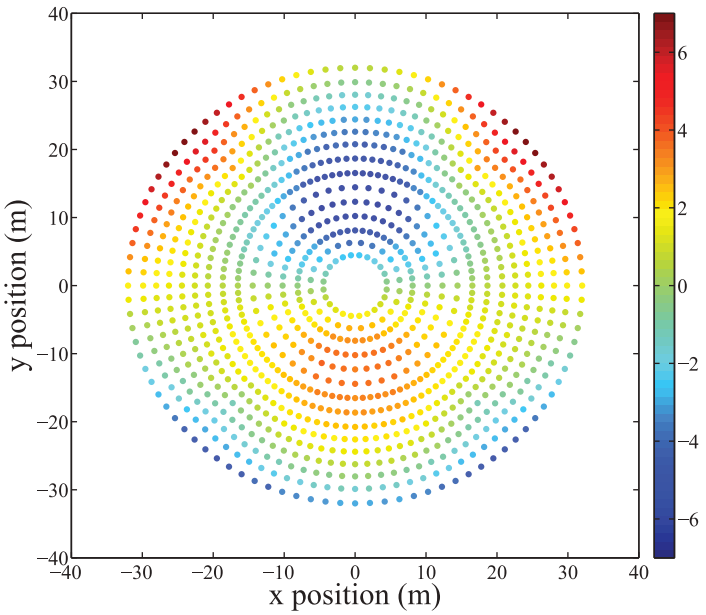

(b) NTS model

Figure 16. Actuator displacements estimated by means of FE models for 90° elevation (the unit of the chromatic scale is m).

In addition, the authors report below a series of fields where an improved numerical model can be profitably used:

- *Buckling problems*, such as those described by Pignataro and Luongo [45–47], Pignataro et al. [49] and Bersani et al. [48] and the papers cited therein. These problems are very sensitive to the stress level achieved and therefore could benefit from its accurate description.
- *New materials* require refined mathematical models to describe them; some authors use suitable parameters [50–53], paying particular attention to cases which leads to non-unique and non-stable solutions [54–56]; alternatively, there is the way followed in dell'Isola and Romano [57] and D'Annibale and Luongo [58] where a concentrated damage model for an interfacial zone is developed; in addition, the application of higher continuum models can be attractive [59–63].

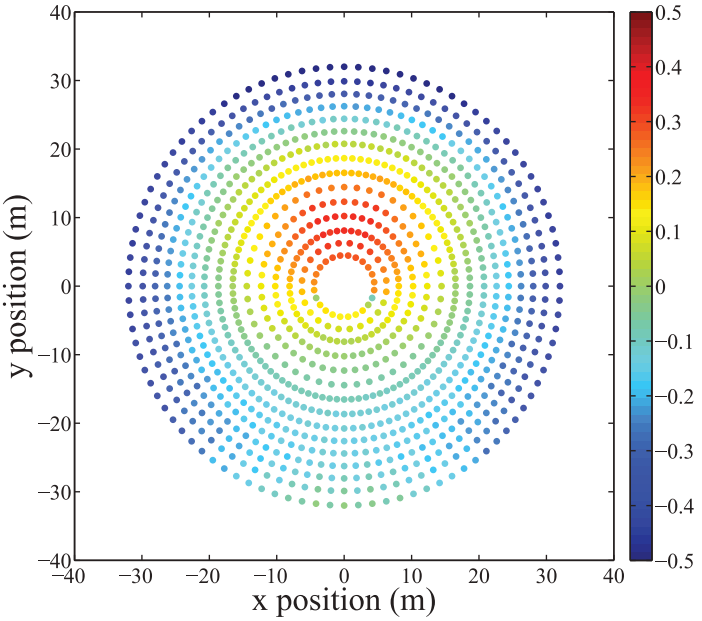

Figure 17. Difference of actuator displacements predicted by the TS and NTS FE models at 15° elevation, $\Delta_{\mathrm{RMS}} = 0.212$ mm (the unit of the chromatic scale is mm).

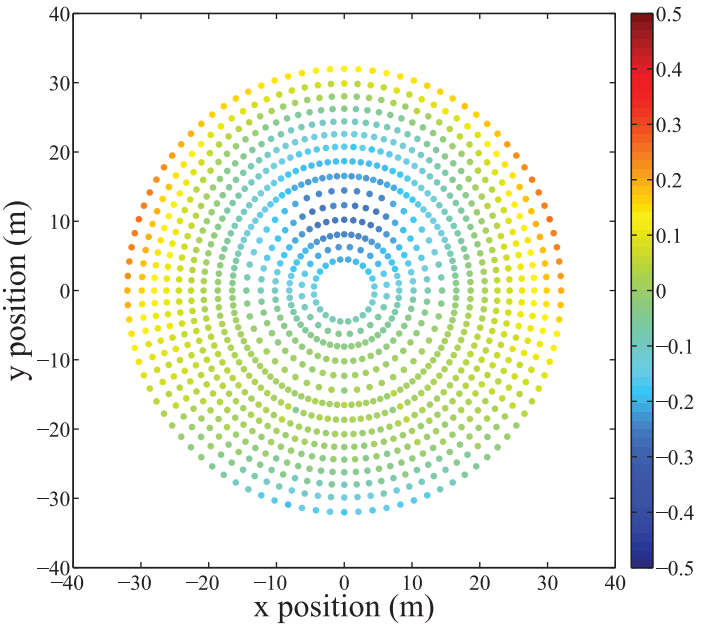

Figure 18. Difference of actuator displacements predicted by the TS and NTS FE models at 60° elevation, $\Delta_{\mathrm{RMS}} = 0.109$ mm (the unit of the chromatic scale is mm).

- *Damage detection* is an emerging and important field which deserves particular attention, see for example the works by Roveri and Carcaterra [64] and Ferretti and Piccardo [65] which consider traveling loads as signals or in identification problems [66–71].
- *Plasticity problems* regarding the evaluation of the collapse load [72–77] and the variational techniques presented in dell'Isola et al. [78] for dissipative phenomena.
- *Smart and piezoelectric materials* might be advantageously used for effective structural control, see Maurini et al. [79], Batra et al. [81], Giorgio et al. [80] and Giorgio et al. [31] for a recent review of relevant results.

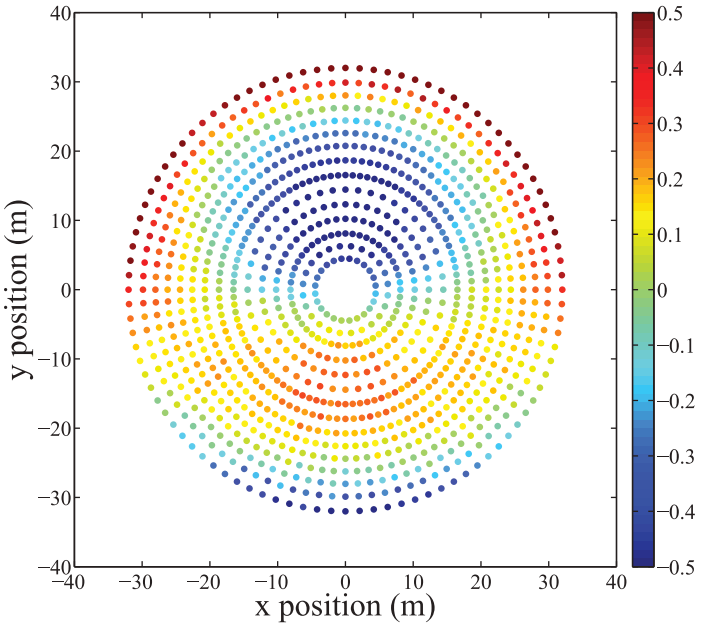

Figure 19. Difference of actuator displacements predicted by the TS and NTS FE models at 90° elevation, $\Delta_{RMS} = 0.271$ mm (the unit of the chromatic scale is mm).

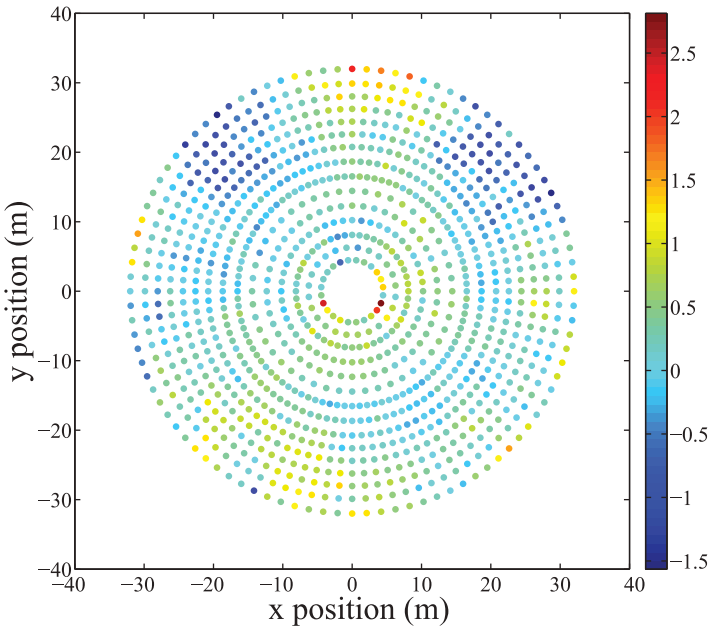

Figure 20. Difference of actuator displacements predicted by the NTS FE model and CRP at 15° elevation, $\Delta_{RMS} = 0.507$ mm (the unit of the chromatic scale is mm).

Declaration of Conflicting Interests

The author(s) declared no potential conflicts of interest with respect to the research, authorship, and/or publication of this article.

Funding

The author(s) disclosed receipt of the following financial support for the research, authorship, and/or publication of this article: The financial support of RAS, the Autonomous Region of Sardinia (grant number CRP-26658, L. R. 7/2007, year 2011 call, Project: *Deformation estimates of the Sardinia Radio Telescope*) is gratefully acknowledged.

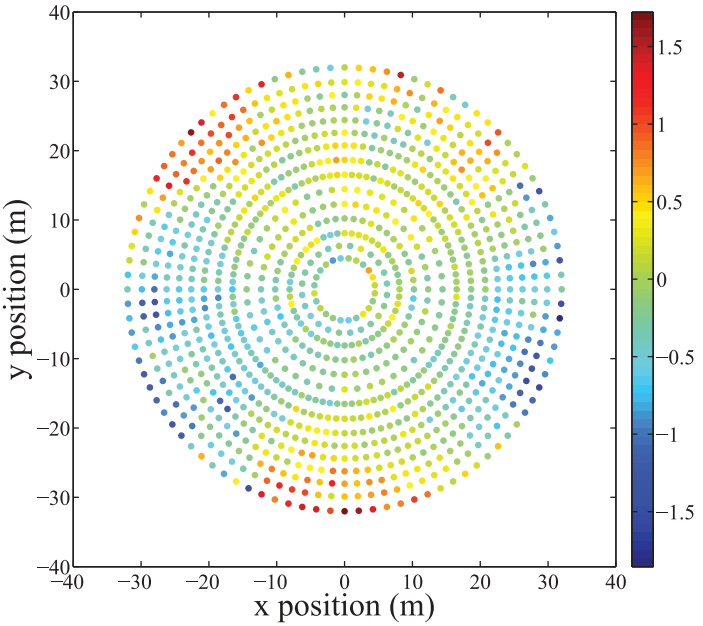

Figure 21. Difference of actuator displacements predicted by the NTS FE model and CRP at 60° elevation, $\Delta_{RMS} = 0.491$ mm (the unit of the chromatic scale is mm).

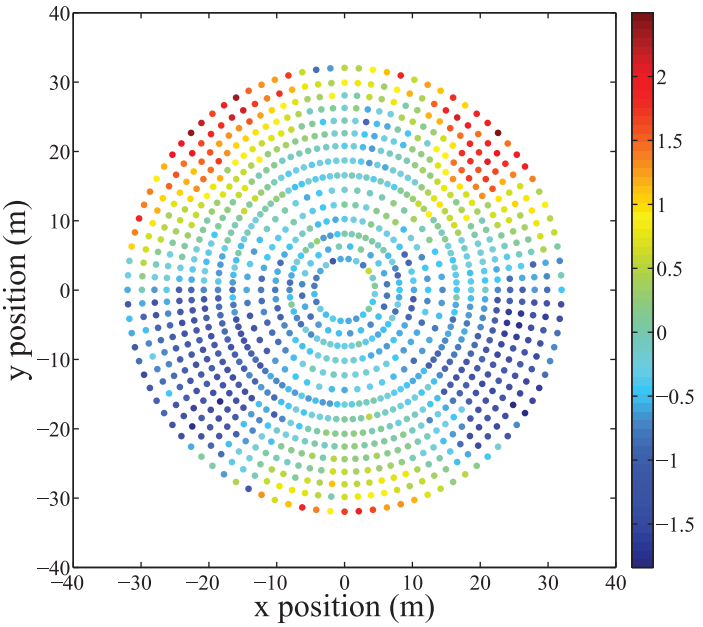

Figure 22. Difference of actuator displacements predicted by the NTS FE model and CRP at 90° elevation, $\Delta_{RMS} = 0.814$ mm (the unit of the chromatic scale is mm).

References

[1] Baars, JWM. *The paraboloidal reflector antenna in radio astronomy and communication*. New York: Springer, 2007.

[2] Ruze, J. Antenna tolerance theory—a review. *Proc IEEE* 1966; 54: 633–640.

[3] Findlay, JW. Antennas, and receivers for radio astronomy. *Adv Radio Res* 1964; 2: 37–119.

[4] Süss, M, Koch, D, and Paluszek, H. The Sardinia Radio Telescope (SRT) optical alignment. *Proc SPIE* 2012; 8444: 84442G.

[5] D'Amico, N. Private communication, 2012.

[6] Zacchiroli, G, Fiocchi, F, Maccaferri, G et al. The panels for primary and secondary mirror reflectors and the active surface system for the new Sardinia Radio Telescope. *Mem Soc Astron Ital* 2006; 10: 126–130.

[7] Luhmann, T, Robson, S, Kyle, S et al. *Close range photogrammetry principles, techniques and applications*. Dunbeath, Scotland: Whittles Publishing, Dunbeath, Scotland 2006.
[8] Zienkiewicz, OC. *The finite element method*. London: McGraw-Hill, 1977.
[9] Besl, PJ, and McKay, ND. A method for registration of 3-D shapes. *IEEE Trans Pattern Anal Mach Intell* 1992; 14: 239–256.
[10] Simo, JC, and Taylor, RL. Consistent tangent operators for rate-independent elastoplasticity. *Comput Meth Appl Mech Eng* 1985; 48: 101–118.
[11] Friswell, MI, and Mottershead, JE. *Finite element model updating in structural dynamics*. New York: Kluwer Academic Publisher, 1995.
[12] Aktan, A, Catbas, N, Türer, N et al. Structural identification: Analytical aspects. *J Struct Eng* 1998; 124: 817–829.
[13] De Sortis, A, Antonacci, E, and Vestroni, F. Dynamic identification of a masonry building using forced vibration tests. *Eng Struct* 2005; 27: 155–165.
[14] Wang, Y, and Zhang, T. Finite element model updating using estimation of distribution algorithms. In: *60th international conference on structural health monitoring of intelligent infrastructure*, Hong Kong, 9–11 December 2013.
[15] Dilena, M, and Morassi, A. Dynamic testing of damaged bridge. *Mech Syst Signal Process* 2011; 25: 1485–1507.
[16] Dilena, M, Morassi, A, and Perin, M. Dynamic identification of a reinforced concrete damaged bridge. *Mech Syst Signal Process* 2011; 25: 2990–3009.
[17] Morassi, A. Dynamic testing and structural identification of the Hypo Bank office complex. I: Experiments. *J Struct Eng ASCE* 2011; 137: 1527–1539.
[18] Morassi, A, and Polentarutti, F. Dynamic testing and structural identification of the Hypo Bank office complex. II: Identification. *J Struct Eng ASCE* 2011; 137: 1540–1552.
[19] Bennati, S, Nardini, L, and Salvatore, W. Dynamic behavior of a medieval masonry bell tower. Part I: Experimental measurements and modeling of bell's dynamic actions. *J Struct Eng* 2005; 131: 1647–1655.
[20] Moaveni, B, and Behmanesh, I. Effects of changing ambient temperature on finite element model updating of the Dowling Hall Footbridge. *Eng Struct* 2012; 43: 58–68.
[21] Richard, B, Adelaide, L, Cremona, C et al. A methodology for robust updating of nonlinear structural models. *Eng Struct* 2012; 41: 356–372.
[22] Zárate, BA, and Caicedo, JM. Finite element model updating: Multiple alternatives. *Eng Struct* 2008; 30: 3724–3730.
[23] Schlune, H, Plos, M and Gylltoft, K. Improved bridge evaluation through finite element model updating using static and dynamic measurements. *Eng Struct* 2009; 31: 1477–1485.
[24] Stochino, F, Cazzani, A, Poppi, S et al. Sardinia Radio Telescope finite element model updating by means of photogrammetric measurements. *Math Mech Solids*. Epub ahead of print January 2014. DOI: 10.1177/1081286515616046.
[25] Turco, E. Load distribution modelling for pin-jointed trusses by an inverse approach. *Comput Meth Appl Mech Eng* 1998; 165: 291–306.
[26] Turco, E. A boundary elements approach to identify static boundary conditions in elastic solids from stresses at internal points. *Inv Probl Eng* 1999; 7: 309–333.
[27] Turco, E. Is the statistical approach suitable for identifing actions on structures? *Comput Struct* 2005; 83: 2112–2120.
[28] Turco, E. Identification of axial forces on statically indeterminate pin-jointed trusses by a nondestructive mechanical test. *Open Civ Eng J* 2013; 7: 50–57.
[29] Tikhonov, AN, and Arsenin, VY. *Solution of ill-posed problems*. New York: John Wiley & Sons, 1977.
[30] Golub, GH and Van Loan, CF. *Matrix computations*. Baltimore: Johns Hopkins University Press, 1996.
[31] Giorgio, I, Galantucci, L, Della Corte, A et al. Piezo-electromechanical smart materials with distributed arrays of piezoelectric transducers: Current and upcoming applications. *Int J Appl Electromagn Mech*. 2015; 47: 1051–1084.
[32] Hansen, PC. Numerical tools for analysis and solution of Fredholm integral equations of the first kind. *Inv Probl* 1992; 8: 849–872.
[33] Pellegrino, S. Structural computations with the singular value decomposition of the equilibrium matrix. *Int J Solids Struct* 1993; 30: 3025–3035.
[34] Golub, GH, Health, M and Wahba, G. Generalized cross-validation as a method for choosing a good ridge parameter. *Technometrics* 1979; 21: 215–223.
[35] Bilotta, A, and Turco, E. A numerical study on the solution of the Cauchy problem in elasticity. *Int J Solids Struct* 2009; 46: 4451–4477.
[36] Turco, E. An effective algorithm for reconstructing boundary conditions in elastic solids. *Comput Meth Appl Mech Eng* 2001; 190: 3819–3829.
[37] Cazzani, A, Malagù, M, and Turco, E. Isogeometric analysis of plane curved beams. *Math Mech Solids*. Epub ahead of print 20 April 2014. DOI: 10.1177/1081286514531265.
[38] Cazzani, A, Malagù, M, Stochino, F et al. Constitutive models for strongly curved beams in the frame of isogeometric analysis. *Math Mech Solids*. Epub ahead of print 31 March 2015. DOI: 10.1177/1081286515577043.
[39] Atluri, SN, and Cazzani, A. Rotations in computational solid mechanics. *Arch Comput Meth Eng* 1995; 2: 49–138.
[40] Cazzani, A, and Atluri, SN. Four-noded mixed finite elements, using unsymmetric stresses, for linear analysis of membranes. *Comput Mech* 1993; 11: 229–251.

[41] Cazzani, A, and Lovadina, C. On some mixed finite element methods for plane membrane problems. *Comput Mech* 1997; 20: 560–572.

[42] Cazzani, A, Garusi, E, Tralli, A et al. A four–node hybrid assumed-strain finite element for laminated composite plates. *Comput Mater Continua* 2005; 2: 23–38.

[43] Cazzani, A, Malagù, M, and Turco, E. Isogeometric analysis: a powerful numerical tool for the elastic analysis of historical masonry arches. *Continuum Mech Thermodyn*. Epub ahed of print 28 December 2014. DOI: 10.1007/s00161-014-0409-y.

[44] Bilotta, A, Formica, G, and Turco, E. Performance of a high-continuity finite element in three-dimensional elasticity. *Int J Numer Meth Biomed Eng* 2010; 26: 1155–1175.

[45] Pignataro, M, and Luongo, A. Asymmetric interactive buckling of thin-walled columns with initial imperfections. *Thin-Walled Struct* 1987; 5: 365–382.

[46] Luongo A. Mode localization in dynamics and buckling of linear imperfect continuous structures. *Nonlinear Dyn* 2001; 25: 133–156.

[47] Luongo, A On the amplitude modulation and localization phenomena in interactive buckling problems. *Int J Solids Struct* 1991; 27: 1943–1954.

[48] Bersani, AM, Giorgio, I, and Tomassetti, G. Buckling of an elastic hemispherical shell with an obstacle. *Continuum Mech Thermodyn* 2013; 25: 443–467.

[49] Pignataro, M, Luongo, A and Rizzi, N. On the effect of the local overall interaction on the postbuckling of uniformly compressed channels. *Thin-Walled Struct* 1985; 3: 293–321.

[50] Rinaldi, A, and Placidi, L. A microscale second gradient approximation of the damage parameter of quasi-brittle heterogeneous lattices. *Z Angew Math Mech* 2014; 94: 826–877.

[51] Rinaldi, A. A rational model for 2D disordered lattices under uniaxial loading. *Int J Damage Mech* 2009; 18: 233–257.

[52] Rinaldi, A. Statistical model with two order parameters for ductile and statistical model with two order parameters for ductile and soft fiber bundles in nanoscience and biomaterials. *Phys Rev E* 2011; 83: 046126.

[53] Madeo, A, Placidi, L, and Rosi, G. Towards the design of metamaterials with enhanced damage sensitivity: Second gradient porous materials. *Res Nondestr Eval* 2014; 25: 99–124.

[54] Eremeyev, VA, and Pietraszkiewicz, W. The nonlinear theory of elastic shells with phase transitions. *J Elast* 2004; 74: 67–86.

[55] Yeremeyev, VA, Freidin, AB and Sharipova, LL. The stability of the equilibrium of two-phase elastic solids. *J Appl Math Mech* 2007; 71: 61–84.

[56] Eremeev, VA, Freidin, AB, and Sharipova, LL. Nonuniqueness and stability in problems of equilibrium of elastic two-phase bodies. *Dokl Phys* 2003; 48: 359–363.

[57] dell'Isola, F, and Romano, A. On the derivation of thermomechanical balance equations for continuous systems with a nonmaterial interface. *Int J Eng Sci* 1987; 25: 1459–1468.

[58] D'Annibale, F, and Luongo, A. A damage constitutive model for sliding friction coupled to wear. *Continuum Mech Thermodyn* 2013; 25: 503–522.

[59] dell'Isola, F, Seppecher, P, and Madeo, A. How contact interactions may depend on the shape of Cauchy cuts in *N*th gradient continua: Approach "á la D'Alembert". *Z Angew Math Phys* 2012; 63: 1119–1141.

[60] Alibert, JJ, and Della Corte, A. Second-gradient continua as homogenized limit of pantographic microstructured plates: a rigorous proof. *Z Angew Math Phys*. 2015; 66: 2855–2970.

[61] dell'Isola, F, and Seppecher, P. The relationship between edge contact forces, double forces and interstitial working allowed by the principle of virtual power. *C R Acad Sci, Ser IIb: Mec, Phys, Astron* 1995; 321: 303–308.

[62] Federico, S, Grillo, A, Imatani, S et al. An energetic approach to the analysis of anisotropic hyperelastic materials. *Int J Eng Sci* 2008; 46: 164–181.

[63] Misra, A. Mechanistic model for contact between rough surfaces. *J Eng Mech* 1997; 123: 475–484.

[64] Roveri, N, and Carcaterra, A. Damage detection in structures under travelling loads by the Hilbert–Huang transform. *Mech Syst and Signal Process* 2012; 28: 128–144.

[65] Ferretti, M, and Piccardo, G. Dynamic modeling of taut strings carrying a traveling mass. *Continuum Mech Thermodyn* 2013; 25: 469–488.

[66] Turco, E. A strategy to identify exciting forces acting on structures. *Int J Numer Meth Eng* 2005; 64: 1483–1508.

[67] Alessandrini, G, Bilotta, A, Formica, G et al. Evaluating the volume of a hidden inclusion in an elastic body. *J Comput Appl Math* 2007; 198: 288–306.

[68] Alessandrini, G, Bilotta, A, Formica, G et al. Numerical size estimates of inclusions in elastic bodies. *Inv Probl* 2005; 21: 133–151.

[69] Alessandrini, G, Bilotta, A, Morassi, A et al. Computing volume bounds of inclusions by EIT measurements. *J Sci Comput* 2007; 33: 293–312.

[70] Wang, Y, and Hao, H. Damage identification scheme based on compressive sensing. *J Comput Civ Eng* 2014; 29: 04014037.

[71] Bilotta, A, and Turco, E. Numerical sensitivity analysis of corrosion detection. *Math Mech Solids*. Epub ahead of print 21 November 2014. DOI: 10.1177/1081286514560093.

[72] Contro, R, Poggi, C, and Cazzani, A. Numerical analysis of fire effects on beam structures. *Eng Comput* 1988; 5: 53–58.

[73] Cazzani, A, Contro, R, and Corradi, L. On the evaluation of the shakedown boundary for temperature-dependent elastic properties. *Eur J Mech, A: Solids* 1992; 11: 539–550.

[74] Andreaus, U, and Baragatti, P. Cracked beam identification by numerically analysing the nonlinear behaviour of the harmonically forced response. *J Sound Vib* 2011; 330: 721–742.
[75] Cazzani, A, and Rovati, M. Sensitivity analysis and optimum design of elastic-plastic structural systems. *Meccanica* 1991; 26: 173–178.
[76] Turco, E, and Caracciolo, P. Elasto-plastic analysis of Kirchhoff plates by high simplicity finite elements. *Comput Meth Appl Mech Eng* 2000; 190: 691–706.
[77] Neff, P, Sysow, A, and Wieners, C. Numerical approximation of incremental infinitesimal gradient plasticity. *Int J Numer Meth Eng* 2009; 77: 414–436.
[78] dell'Isola, F, Madeo, A, and Seppecher, P. Boundary conditions at fluid–permeable interfaces in porous media: A variational approach. *Int J Solids Struct* 2009; 46: 3150–3164.
[79] Maurini, C, Pouget, J, and dell'Isola, F. Extension of the Euler–Bernoulli model of piezoelectric laminates to include 3D effects via a mixed approach. *Comput Struct* 2006; 84: 1438–1458.
[80] Giorgio, I, Culla, A, and Del Vescovo, D. Multimode vibration control using several piezoelectric transducers shunted with a multiterminal network. *Arch Appl Mech* 2009; 79: 859–879.
[81] Batra, RC, dell'Isola, F, Vidoli, S et al. Multimode vibration suppression with passive two-terminal distributed network incorporating piezoceramic transducers. *Int J Solids Struct* 2005; 42: 3115–3132.